

Parallel Particle Simulation of the Near-Continuum Hypersonic Flows Over Compression Ramps

J.-S. Wu¹

Assistant Professor,
e-mail: chongsin@cc.nctu.edu.tw

K.-C. Tseng

Graduate Student

Department of Mechanical Engineering,
National Chiao-Tung University,
1001 Ta-Hsueh Road,
Hsinchu 30050, Taiwan

This paper describes the analysis of the near-continuum hypersonic flow over a compression ramp using the two-dimensional parallel direct simulation Monte Carlo (DSMC) method. Unstructured and triangular solution-based adaptive mesh depending on the local mean free path is used to improve the resolution of solution for the flow field with highly varying properties. In addition, a freestream parameter is defined to help reduce the cell numbers in the freestream area, resulting in appreciable decrease of the computational time (20–30%) without sacrificing the accuracy of the solution. The two-step multilevel graph partition technique is used for physical domain decomposition, employing estimated particle number distribution in each cell as the graph vertex weight. 32 IBM-SP2 processors are used throughout the study unless otherwise specified. The Effect of the outflow vacuum boundary condition, compression ramp angle, freestream condition, and length of the ramp to the flow field are investigated. Computational results are compared with previous numerical results whenever available.

[DOI: 10.1115/1.1523068]

Introduction

Due to the complicated physical features possessed by hypersonic compression ramp flow and its importance to the design of hypersonic vehicles, it has been studied extensively in the past, [1–6]. Details of the general physics can be found in Refs. [1–6] and references cited therein. Several points, however, are worthy of mentioning here. First, the tip flows are in strong nonequilibrium and hence continuum assumption breaks down in this regime, where the Navier-Stokes equation fails to approximate the flow features. Second, most flows relevant to hypersonic vehicles are in the range of transition to near-continuum, thus the direct simulation Monte Carlo method (DSMC), [7], is well-suited to study this complicated flow field, although the computational cost is extremely high in the near-continuum regime. Third, the flow possesses very complicated physical features involving highly varying flow properties, which are very difficult to resolve using nonadaptive mesh.

In order to well resolve the complicated flow features of a compression ramp using the DSMC method, two issues are required to handle it properly. First, the distribution of computational cells should be adapted to the variation of the flow properties. Hence, solution-based adaptive mesh is generally required. In traditional computational fluid dynamics (CFD), unstructured mesh rather than structured mesh is more flexible for the purpose of mesh adaptation. The same applies to the DSMC method. There were, however, relatively few studies developed along this line, [8,9], in the DSMC community. Robinson [8] first applied the re-meshing technique to adapt the unstructured mesh, then Wu et al. [9] applied the mesh-embedding scheme instead to adapt the unstructured mesh. Second, due to the high computational cost of the DSMC simulation, especially in the near-continuum regime, parallel processing is highly expected. Fortunately, DSMC is readily paralleled using domain decomposition due to its particle nature and high locality due to assumed binary collisions. Detailed reviews of parallel processing of DSMC can be found in Refs. [8,10], which will not be repeated here for brevity.

¹To whom correspondence should be addressed.

Contributed by the Fluids Engineering Division for publication in the JOURNAL OF FLUIDS ENGINEERING. Manuscript received by the Fluids Engineering Division Jan. 2, 2002; revised manuscript received Aug. 20, 2002. Associate Editor: Y. Matsumoto.

As mentioned earlier, the hypersonic flow over a compression ramp involves rather complicated flow phenomena with highly varying flow properties. Hence, integration of parallel processing and unstructured adaptive mesh is highly expected to accelerate the computational speed to an acceptable level as well as to improve the resolution.

Therefore, the specific objectives of the current study are

1. to integrate the previously developed DSMC method using unstructured adaptive mesh, [9], and the parallel DSMC method, [10], using unstructured mesh;
2. to apply this method to compute a hypersonic compression ramp flow and compare the results with those of Moss et al. [6]; and
3. to study the effects of ramp angles, free-stream conditions, outflow vacuum boundary conditions, and ramp length on the flow properties, including pressure, shear stress, and heat transfer coefficients.

The paper begins with descriptions of numerical methods. Results of short compression are compared to those of Moss et al. [6] and different effects on surface properties are discussed in turn.

Numerical Method and Procedures

Parallel Direct Simulation Monte Carlo (DSMC) Method. The DSMC algorithm is readily parallelized through the physical domain decomposition as mentioned previously. The cells of the computational grid are distributed among the processors. Each processor executes the DSMC algorithm in serial for all particles and cells in its own domain. Parallel communication occurs when particles cross the domain (processor) boundaries and then particle data are transferred between processors. Figure 1 shows a simplified flow chart of the parallel DSMC method proposed in the current study. Note that CPUs are numbered from 0 to np-1 in the figure.

In this method, an approach of handling the cell related data is proposed. An unstructured triangular mesh is first constructed using the advancing front method by a commercial code, Hyper-Mesh™, [11]. Then, a preprocessor (or “converter”) is designed to convert the unstructured mesh data into the *globally sequential but locally unstructured* mesh data for each processor in confor-

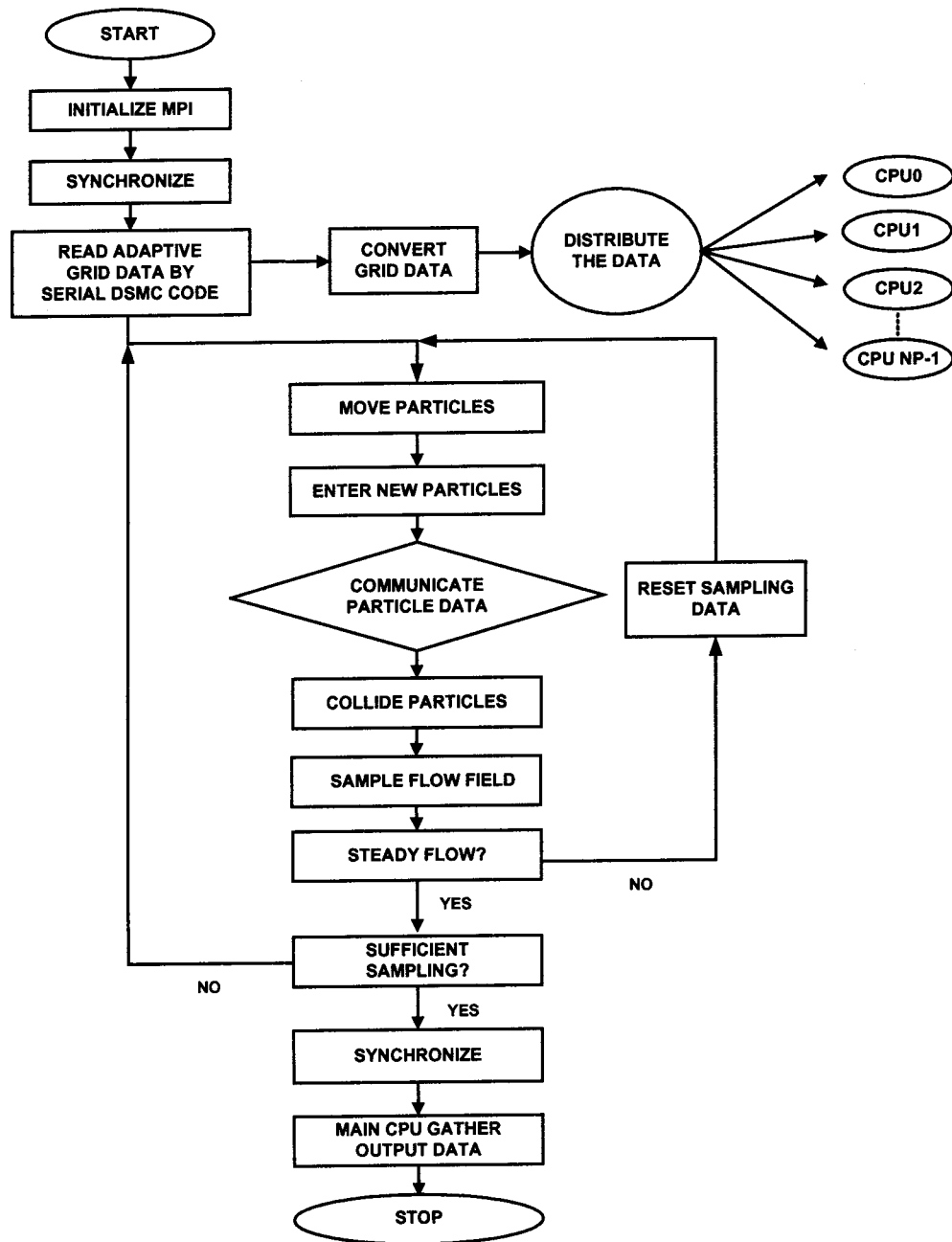


Fig. 1 Flow chart of the parallel DSMC method

mation with the partitioning information from graph partitioner (e.g., JOSTLE [12]), as schematically presented in Fig. 2. In each processor, the cell numbering is unordered (unstructured), but the starting (and ending) cell number increases sequentially with the processor number. We term this as “globally sequential but locally unstructured.” Thus, in each processor the memory is only needed to record the starting and ending cell numbers. This simple conversion dramatically reduces the memory cost otherwise required for storing the mapping between the local cell number in each processor and the global cell number in the computational domain if unstructured cells are used, [10]. The resulting mesh data is then imported into the parallel DSMC code.

After reading the mesh data on a master processor (cpu 0), the mesh data are then distributed to all other processors according to the designated domain decomposition. All the particles in each processor then start to move as in sequential DSMC algorithm.

The particle related data are sent to a buffer and are numbered sequentially when hitting the inter-processor boundary (IPB) during its journey within a simulation time-step. After all the particles in a processor are moved, the destination processor for each particle in the buffer is identified via a simple arithmetic computation, owing to the previously mentioned approach for cell numbering, and the transferred data are then packed into arrays. Considering communication efficiency, the packed arrays are sent as a whole to its surrounding processors, in turn based on the tagged numbers recorded earlier. Once a processor sends out all the packed arrays, it waits to receive the packed arrays from its surrounding processors in turn. This “send” and “receive” operation serves practically as a synchronization step during each simulation time-step. Received particle data are then unpacked and each particle continues to finish its journey for the remaining

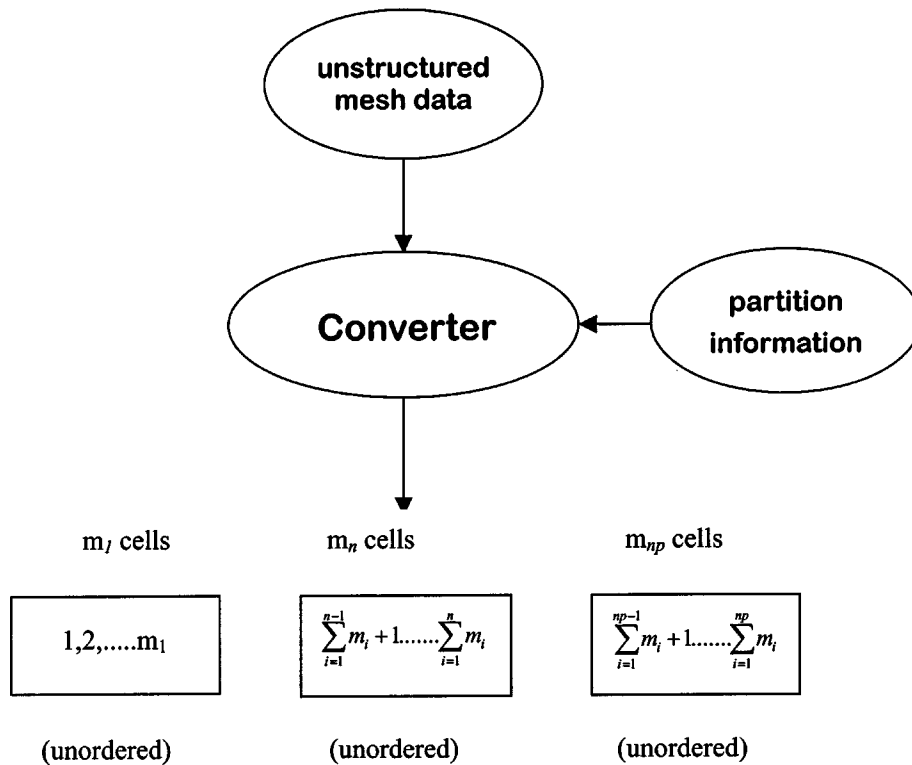


Fig. 2 Cell renumbering scheme in the parallel DSMC method

time-step. The above procedures are repeated twice since there might be some particles crossing the IPB twice during a simulation time-step.

After all particles on each processors have come to their final destinations at the end of a time-step, the program then carries out the indexing of all particles and the collisions of particles in each

computational cell in each processor as usual in a sequential DSMC code. The particles in each cell are then sampled at the appropriate time as specified.

The current parallel code, in SPMD (single program multiple data) paradigm, is implemented on the IBM-SP2 machines (distributed memory system) using the message passing interface (MPI) to exchange information between processors. It is thus essentially no code modification required to adapt to other parallel machines (e.g., IBM-SMP, PC-clusters) with a similar distributed memory system once they use the same MPI libraries for data communication.

The DSMC Method With Mesh Adaptation. All mesh adaptation methods need some means to detect the requirement of local mesh refinement to better resolve the features in the flow fields and hence to achieve more accurate numerical solutions. This also applies to DSMC. It is important for the adaptation parameters to detect a variety of flow features but does not cost too much computationally. Often the gradient of the properties, such as pressure, density, or velocity, is used as the adaptation parameter to detect rapid changes of the flow-field solution in traditional CFD. However, by considering the statistical nature of

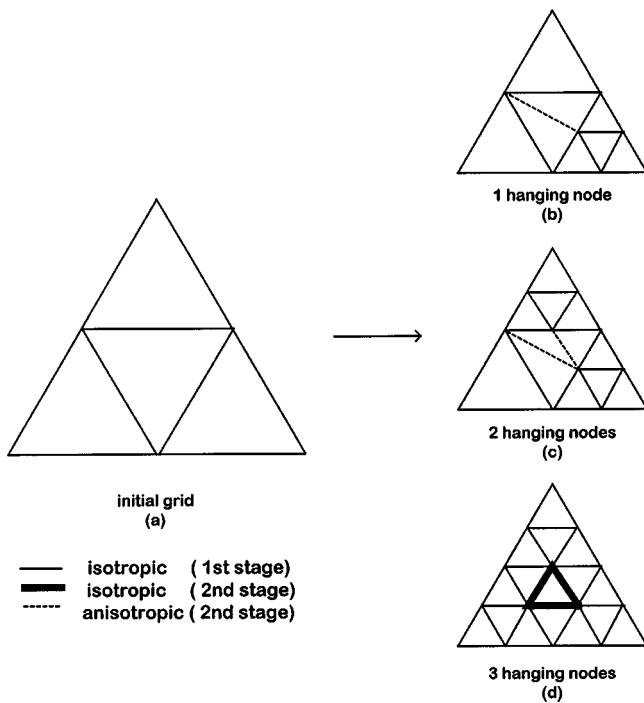


Fig. 3 Mesh refinement scheme for unstructured triangular mesh

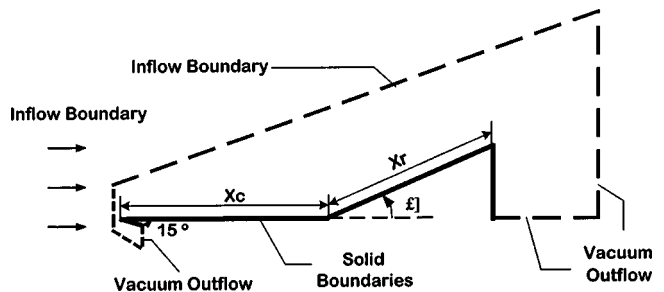


Fig. 4 Sketch of the two-dimensional hypersonic compression corner flow

Table 1 Flow conditions of simulation

Case	x_r (mm)	$\rho_\infty \times 10^{-5}$ (Kg/m ³)	V_∞ (m/s)	T_∞ (K)	T_w (K)	M_∞ (-)	$x_c = 71.4$ mm		
							λ_∞ (mm)	Kn_∞ (-)	Re_∞ (-)
1	31.55	5.14	1340	8.3	383	22.8	0.475	0.0066	3938.66
2	31.55	10.72	1452	8.6	394	24.3	0.230	0.0032	8670.23
3	31.55	18.09	1448	14.1	340	18.9	0.154	0.0022	10120.06
4	31.55	39.12	1740	15.6	341	21.6	0.073	0.0010	24402.49
5	71.4	39.12	1740	15.6	341	21.6	0.073	0.0010	24402.49

the DSMC method, density is adopted instead as the adaptation parameter in the current study. Using density as the adaptation parameter in DSMC is justified since it is generally required that the cell size be much smaller than the local mean free path to better resolve the flow features as advocated by Bird [7]. To use the density as an adaptation parameter, a local cell Knudsen number is defined as

$$Kn_c = \frac{\lambda_c}{\sqrt{A_c}}, \quad (1)$$

where λ_c is the local cell mean free path based on VHS model and A_c is the magnitude of the local cell area. When the mesh adaptation module is initiated, the local Knudsen number at each cell is computed and compared with a preset value, Kn_{cc} . If this value is less than the preset value, then mesh refinement is required. If not, check the next cell until all cells are checked. This adaptation parameter is expected to be most stringent on mesh refinement (more cells are added); hence, the impact to the DSMC computational cost might be high, but it is required to obtain an accurate solution.

Considering the practical applications of mesh adaptation in external flows, we have added another constraint, $\phi \geq \phi_0$, in addition to the constraint of the local cell Knudsen number. Note that the freestream parameter, ϕ , is defined as

$$\phi = \frac{\rho}{\rho_\infty}, \quad (2)$$

where ϕ_0 is a preset value. Not only does the above constraint help to reduce the total refined cell numbers to an acceptable level by reducing the cell numbers in the freestream region a great deal, but it also reduces the total computational time up to 30%.

Two general rules of mesh adaptation are described as follows:

(1) *Isotropic mesh refinement is employed for those cells which flag for mesh refinement.* A new node is added on each edge (face) of a *parent cell* and connecting them to form four *child cells*. In general, this will create one to three hanging nodes in the nonrefined interfacial cell, which is next to the isotropically refined cell. Existence of hanging node(s) not only complicates the particle

movement, but also increases the cost of the cell-by-cell particle tracing due to the increase of face numbers. Hence, a remedy is proposed as follows in item (2).

(2) *Anisotropic mesh refinement is utilized in the (interfacial) cells next to those cells have just been isotropically refined.* Triangular child cells are formed no matter how many hanging nodes exist. Typical methods of interfacial mesh refinement in the triangular cells are schematically shown in Fig. 3.

The mesh adaptation procedures are performed using a serial DSMC code using very few particles (<1%). As a rule of thumb, about 10,000 particles sampled in a cell are considered enough for the mesh adaptation purpose. The mesh adaptation module is initiated and checks through all the cells to determine if mesh enrichment is required based on the specific adaptation parameter, which was explained previously. If mesh enrichment is conducted, associated neighbor identifying arrays are updated or created, coordinates and number of faces for new cells are recorded, and sampled data on the coarse *parent cell* are redistributed (based on the magnitude of cell area) to the finer *child cells* accordingly. The above procedures are repeated until the prescribed maximum number of adaptation levels has been reached or no mesh enrichment is required for all the cells in the computational domain. Finally the adaptive mesh due to the above procedures is outputted as the computational cells for further parallel DSMC processing. In summary, output adaptive mesh and density distribution is then used as the information for domain decomposition using the graph partitioner, JOSTLE, [12]. Finally, the previously developed parallel DSMC code, [10], is then utilized for computation.

Results and Discussion

Figure 4 illustrates the sketch of a hypersonic flow over a compression ramp as previously simulated by Moss et al. [6]. Current flow conditions are summarized in Table 1, where cases 1–4 ($x_c = 71.4$ mm, $x_r = 31.55$ mm) corresponds to those simulated in Moss et al. [6] except for case 5 ($x_c = 71.4$ mm, $x_r = 71.4$ mm) with a longer ramp. For completeness, they are briefly described here as follows: VHS nitrogen gas, freestream Mach number $M_\infty = 18.9 \sim 24.3$, freestream density $\rho_\infty = 5.14E-5 \sim 39.12E-5$ Kg/m³, freestream temperature $T_\infty = 8.3 \sim 15.6$ K, and a fully thermally accommodated and diffusive flat and ramp wall

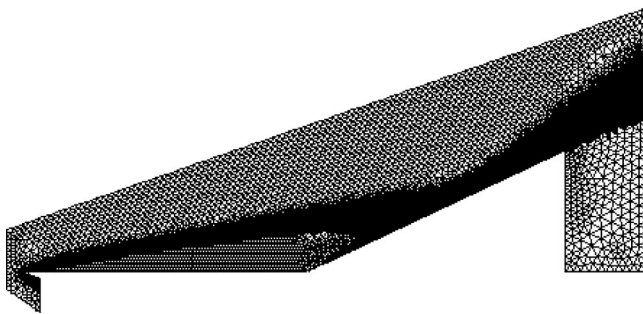


Fig. 5 Unstructured adaptive mesh for case 5 ($x_r = 71.4$ mm, $\beta = 25$ deg) (163,658 cells, 3 levels of mesh adaptation)

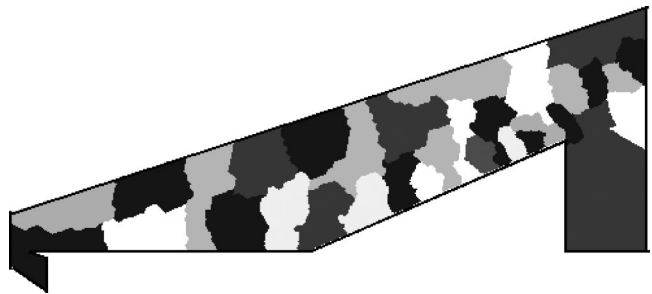


Fig. 6 Multilevel graph partition for case 5 ($x_r = 71.4$ mm, $\beta = 25$ deg) (32 CPUs)

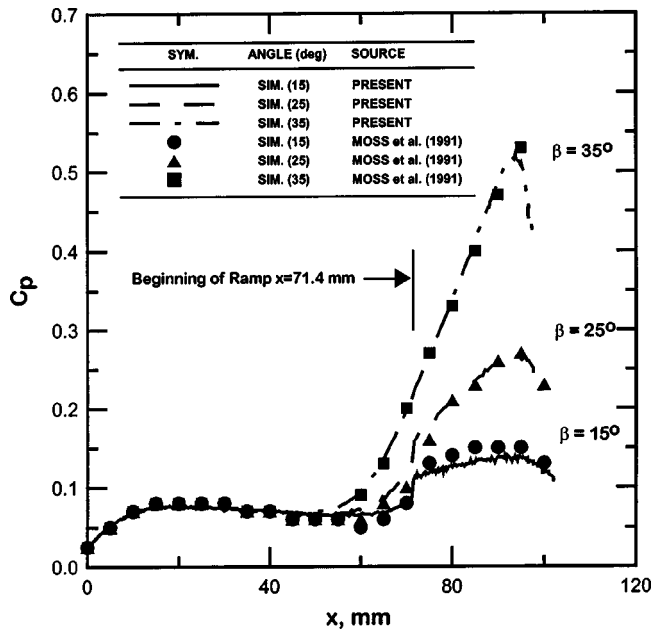


Fig. 7 Pressure coefficient distribution along the solid wall for $\beta=15$ deg, 25 deg, and 35 deg (case 1, $Kn_\infty=0.0066$)

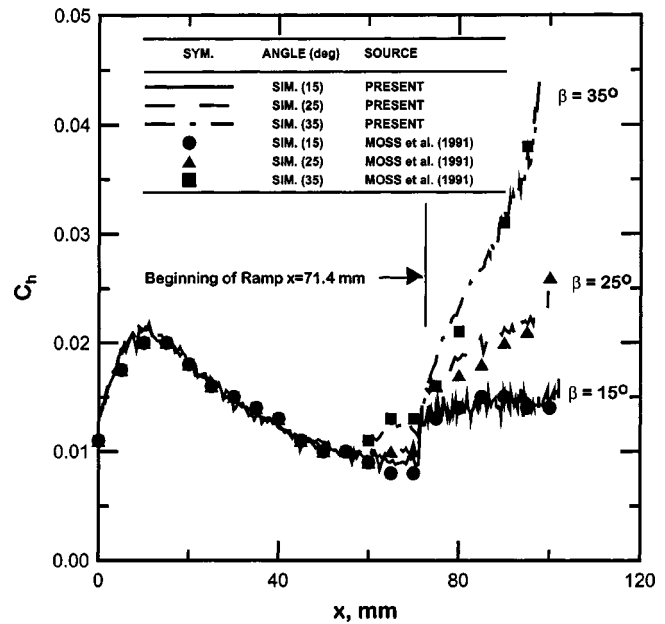


Fig. 9 Heat transfer coefficient distribution along the solid wall for $\beta=15$ deg, 25 deg, and 35 deg (case 1, $Kn_\infty=0.0066$)

with $T_w=340\sim 394$ K. The resulting Knudsen numbers and Reynolds numbers based on x_c are in the range of 0.0010–0.0066 and 3938.66–24402.49, respectively. Temperature-dependent rotational energy exchange model of Parker [7] is used to model the diatomic nitrogen gas. Vibration energy transfer is neglected due to the low temperature involved. Typical particle numbers and cell numbers are in the range of 0.8–8 million and 19,000–250,000, respectively, depending upon the rarefaction of the problem. Additionally, ϕ_0 is normally set to 1.03 unless otherwise specified. Typical adaptive mesh distribution is shown in Fig. 5 for the case 5 at ramp angle of 25 deg (163,658 cells). Corresponding distribution for domain decomposition using the graph-partitioning technique is illustrated in Fig. 6. Note that the size of each sub-domain is obviously different due to the variations of estimated

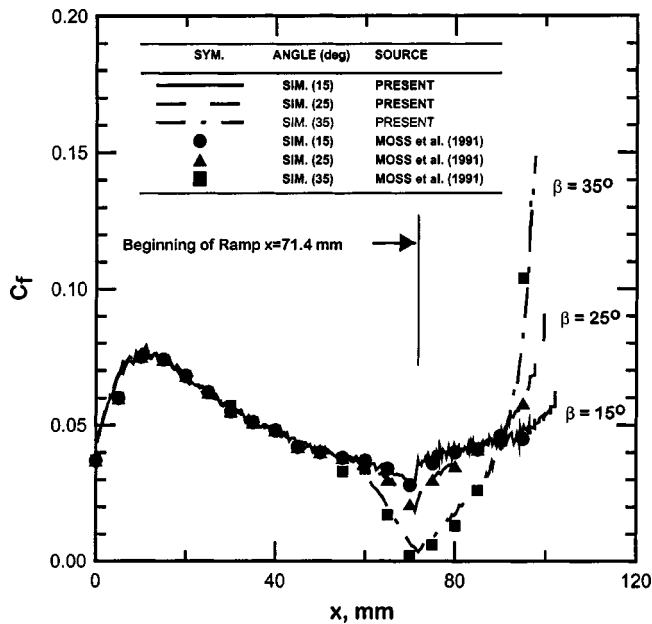


Fig. 8 Shear stress coefficient distribution along the solid wall for $\beta=15$ deg, 25 deg, and 35 deg (case 1, $Kn_\infty=0.0066$)

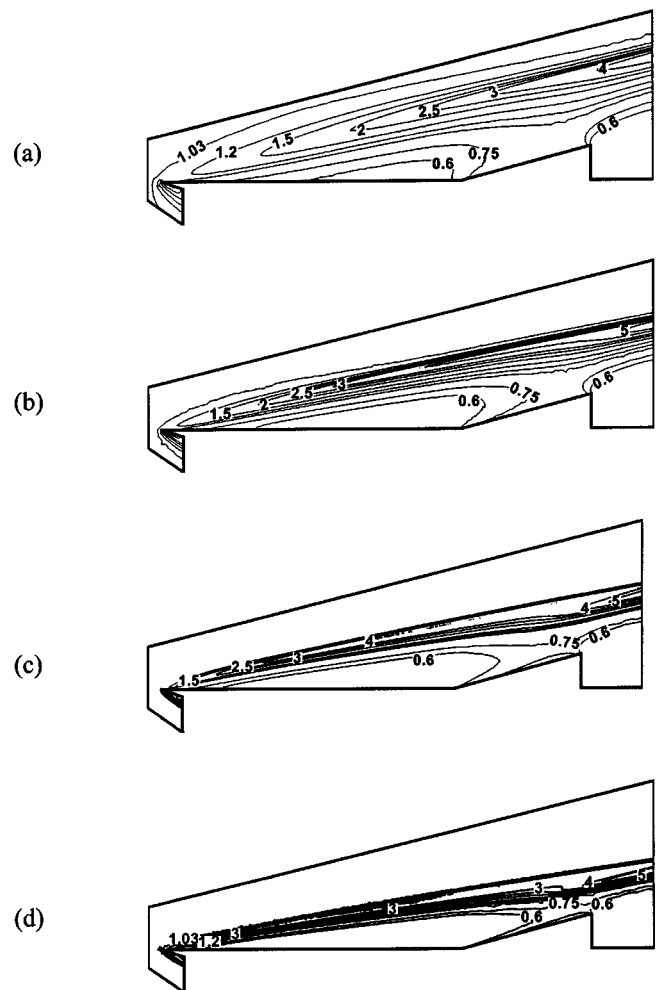


Fig. 10 Density contours at different freestream Knudsen number for $\beta=15$ deg (a) $Kn_\infty=0.0066$; (b) $Kn_\infty=0.0032$; (c) $Kn_\infty=0.0022$; (d) $Kn_\infty=0.0010$

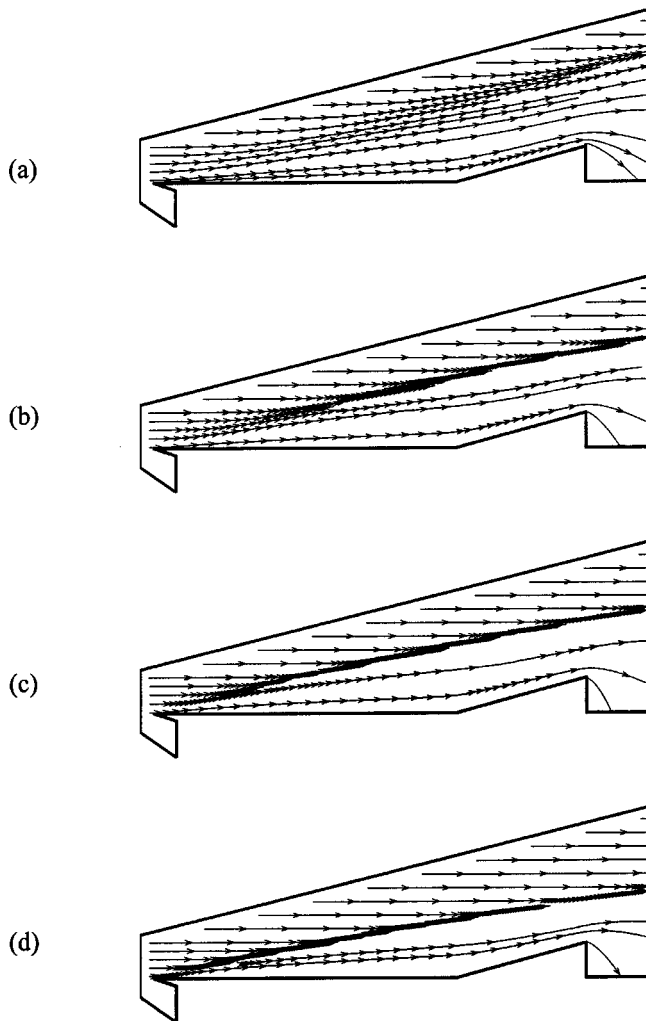


Fig. 11 Streamline contours at different freestream Knudsen number for $\beta=15$ deg (a) $Kn_\infty=0.0066$; (b) $Kn_\infty=0.0032$; (c) $Kn_\infty=0.0022$; (d) $Kn_\infty=0.0010$

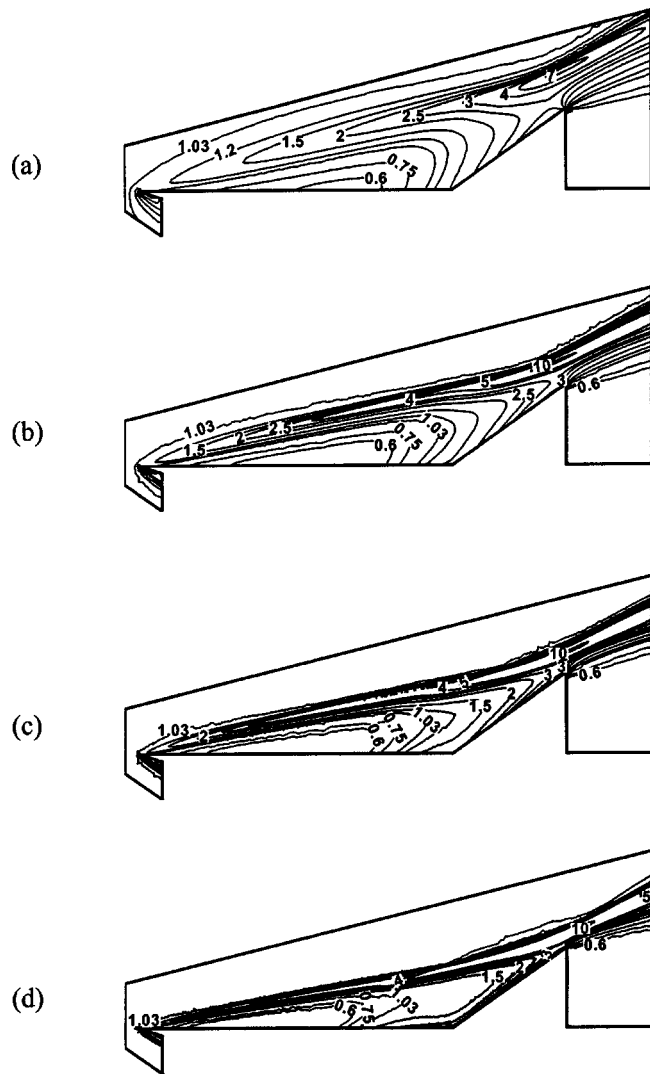


Fig. 12 Density contours at different freestream Knudsen number for $\beta=35$ deg (a) $Kn_\infty=0.0066$; (b) $Kn_\infty=0.0032$; (c) $Kn_\infty=0.0022$; (d) $Kn_\infty=0.0010$

density distribution (or equivalently computational load) in the computational domain. Note that 32 IBM-SP2 processors are used throughout the current study unless otherwise specified.

Verification of the Present Implementation. In Moss et al. [6], the outflow vacuum condition was placed right at the end of the ramp instead of the current position as shown in Fig. 4. It was, however, problematic since previous results showed a large circulation bubble formed at the compression corner for a large ramp angle with the flow reattached near the end of the ramp. This might cause subsonic outflow (or even reversed flow) near the end of the ramp wall, which renders the vacuum outflow conditions unphysical. In the current study, we have moved the outflow vacuum boundary condition further downstream to the wake region as shown in Fig. 4, which coincides more with the experimental conditions, [6].

Figures 7, 8, and 9 illustrate the pressure, shear stress, and heat transfer coefficient distribution, respectively, along the solid wall for case 1 (the most rarefied case in Table I with a short ramp) at three different ramp angles (15 deg, 25 deg, and 35 deg). Detailed discussion on the physics of the flow field is relatively brief since it can be found in Moss et al. [6]. As shown in Fig. 7, the pressure distribution generally increases with the distance from the leading edge, reaches a maximum value 0.077 at approximately the position of $x=20$ mm, and then decreases to some value before the ramp corner, depending upon the ramp angle. Pressure increases

appreciably starting from the corner region due to the existence of ramp, especially for the 35 deg case. For the cases considered, the data generally coincide very well with those of Moss et al. [6] except at the end of the ramp for the 35 deg case, due to the position of outflow vacuum condition. Current prediction shows that strong expansion occurs in this regime for the 35 deg case, which will be shown later. This is reasonable since the flow close to the end of the ramp wall is slowed down most due to the large angle of the ramp corner although no reverse flows occur. The placement of the outflow vacuum boundary condition in Ref. [6] will prevent the flow from expanding at this regime. In addition, shear stress and heat transfer coefficient distributions for all three ramp angles (Fig. 8) along the solid wall agree reasonably well with those of Moss et al. [6]. The current cell numbers for this case is on the order of 20,000, which is larger than that used by Moss et al. [6] ($\approx 7,000$). But the distribution of cells is definitely better due to the solution-based adaptive mesh. Also the particle numbers is about 0.8–2 million that is much larger than that (≈ 0.1 – 0.2 million) used in Ref. [6]. This represents that the current parallel DSMC simulation using unstructured adaptive mesh is at least as accurate as (or may be more accurate than) previous simulation study for the most rarefied case.

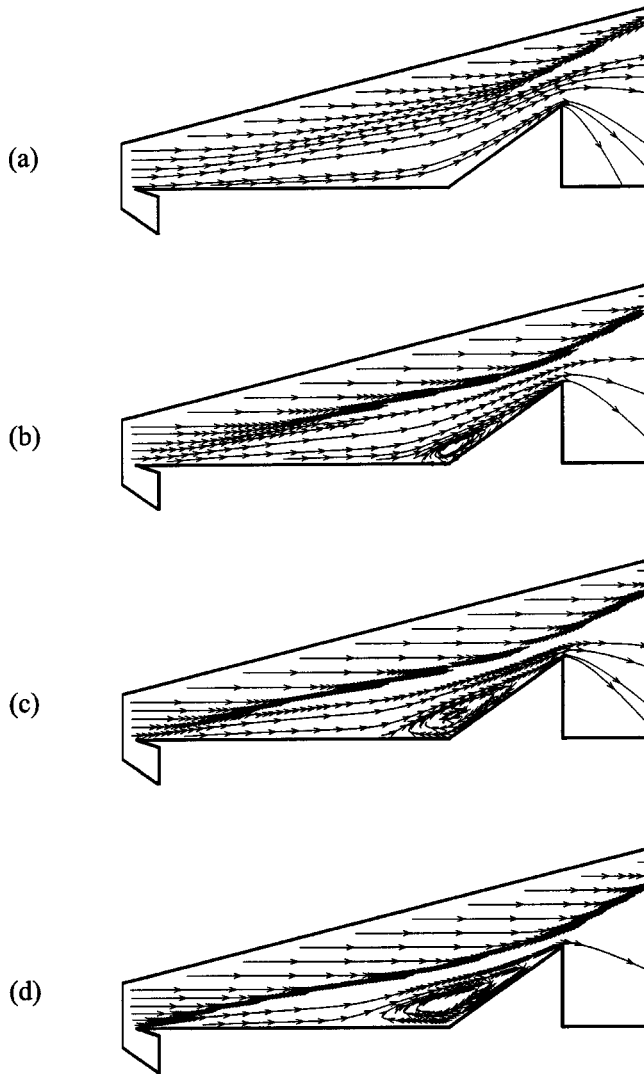


Fig. 13 Streamline contours at different freestream Knudsen number for $\beta=35$ deg (a) $Kn_\infty=0.0066$; (b) $Kn_\infty=0.0032$; (c) $Kn_\infty=0.0022$; (d) $Kn_\infty=0.0010$

Effects of Freestream Rarefaction and Ramp Angle. Effects of rarefaction for the short ramp can be clearly demonstrated in Figs. 10, 11 (15 deg) and Figs. 12, 13 (35 deg). In Figs. 11(a)–11(d) ($\beta=15$ deg, density distribution), the density gradient across the leading-edge shock increases with decreasing freestream rarefaction. In addition, rarefied region above the flat-plate increases with decreasing freestream rarefaction as well. In addition, strong gas expansion occurs at the end of the ramp wall, which causes the pressure to decrease as shown earlier in Fig. 7. Because of the short ramp length considered, the oblique shock due to compression corner is not very clearly formed even in the case of the densest flow (Fig. 11(d)). No separation bubble can be identified for all the cases considered with ramp angle of 15 deg (Figs. 11(a)–11(d), streamline contour). From Figs. 11(b)–11(d), the leading-edge shock extends over the ramp due to the very blur (weak) oblique shock. Additionally, the strength of the leading-edge shock increases with decreasing rarefaction as expected.

In Figs. 12(a)–12(d) ($\beta=35$ deg, density distribution), physical trend for density distribution is similar to those of 15 deg as shown in Fig. 10. There is, however, one distinct feature caused by the large ramp angle. Density in the corner region is more uniform than that of 15 deg case as compared with Figs. 10(a)–10(d). This is caused by the circulation bubble formed in the com-

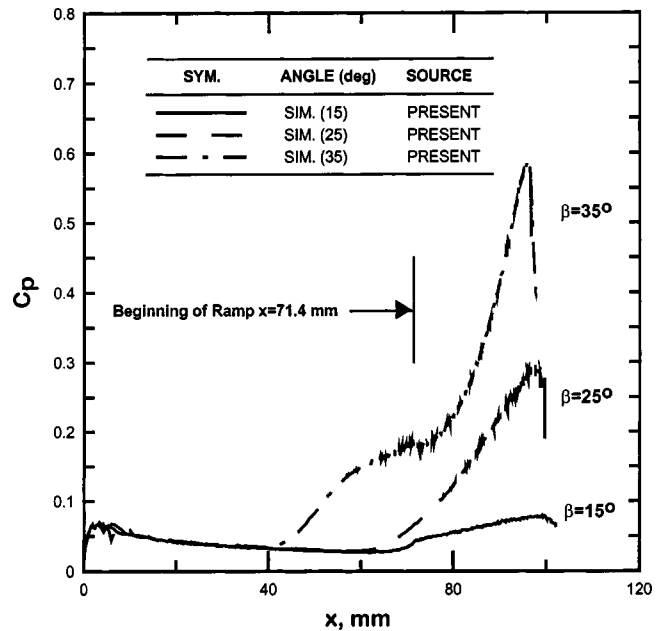


Fig. 14 Pressure coefficient distribution along the solid wall for $\beta=15$ deg, 25 deg, and 35 deg (case 4, $Kn_\infty=0.0010$)

pression corner as shown in Figs. 13(a)–13(d) for lower freestream rarefaction cases. In addition, the gas expansion at the end of the ramp wall is more obvious as compared with that of the 15 deg case, which is expected due to the adverse pressure gradient along the ramp caused by the large ramp angle. From both Figs. 12 and 13, the leading-edge shock is deflected upwards and mingled with oblique shock (due to the corner) at the end of the ramp due to the large ramp angle. Note that the oblique shock due to the ramp corner is not very clear because of the short ramp. In addition, the size of the separation bubble increases with decreasing rarefaction. The separation bubble even extends over 1/3 upstream of the flat-plate length and almost covers the entire ramp

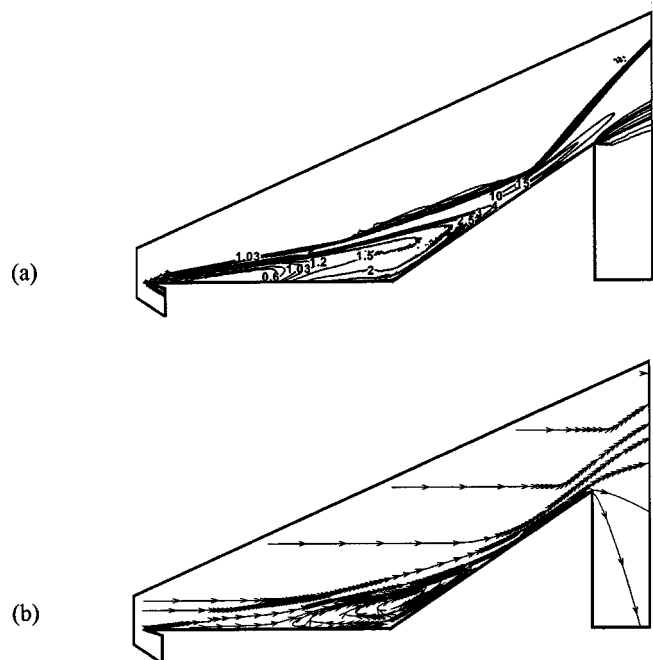


Fig. 15 Density and streamline contours at $\beta=35$ deg (long ramp, case 5, $Kn_\infty=0.0010$)

wall. This definitely will dramatically change the surface properties as can be seen, for example, in Fig. 14, where the pressure coefficient is much higher in the corner region for the $\beta=35$ deg case as compared with the other two cases ($\beta=15$ deg and 25 deg).

Generally speaking, the strength of leading-edge shock, gas expansion at the end of the ramp, as well as the separation bubbles size in the corner increases with decreasing rarefaction.

Effects of Length of the Ramp. Effects of the ramp length on the flow structure can be illustrated in Fig. 15, where $\text{Kn}_\infty = 0.001$ (case 5, $x_r = 71.4$ mm, $\beta = 35$ deg) which is in the near-continuum regime. The formation of the strong oblique shock is very clear at the later portion of the ramp due to the longer ramp considered. For the short ramp case at the same angle (Fig. 12(d)), the oblique shock is comparably blurred due to the short ramp. In addition, the gas expansion fan the corner of the ramp (to the wake region) is clearly seen because of the formation of the strong oblique shock. A well-known neck region is clearly formed along the ramp wall. Comparing Fig. 15(b) and Fig. 13(d), we can see that the circulation bubble is larger because of the long ramp. Hence, the rarefied region above the flat-plate (as compared with the freestream value) becomes smaller due to the large circulation bubble. The nature of the interaction among the leading-edge shock, the viscous boundary layer along the solid wall and the oblique shock is rather complicated. The related discussion can be found in Robinson [8] and are skipped here.

Conclusions

A two-dimensional parallel DSMC method using unstructured solution-based adaptive mesh has been developed. Simulated data of a hypersonic flow over a compression ramp at a most rarefied condition are used to compare with previous reported results. It is then applied to simulate similar flow to study the effects of the freestream rarefaction, ramp angle, and the effects of the ramp length. This study shows that simulation of near-continuum flow using the DSMC method is possible using parallel processing. Future work considering dynamic load balancing during simulation for parallel DSMC is in progress and will be reported elsewhere.

Acknowledgment

This investigation was supported by the National Science Council of Taiwan, Grant No. NSC 90-2212-E-009-046. The authors also would like to express their sincere thanks to the computing resources provided by the National Center for High-Speed Computing of National Science Council of Taiwan.

Nomenclature

a_∞	=	freestream sound speed
C_w	=	shear stress coefficient, $2\tau_w/\rho_\infty V_\infty^2$
C_p	=	pressure coefficient, $2p_w/\rho_\infty V_\infty^2$
C_h	=	heat transfer coefficient, $2q_w/\rho_\infty V_\infty^3$
Kn_∞	=	freestream Knudsen number, λ_∞/x_c
M_∞	=	freestream Mach number, U_∞/a_∞
p	=	pressure
q	=	heat transfer rate
$\text{Re}_{\infty,x}$	=	local Reynolds number, $\rho_\infty V_\infty x/\mu_\infty$
T	=	temperature
T_{tr}	=	translational temperature
U_∞	=	freestream velocity
x_c	=	distance from leading edge to the ramp corner
x_r	=	ramp length
β	=	ramp angle
λ_∞	=	mean-free path in freestream
μ	=	viscosity
ρ	=	density
τ	=	shear stress

Subscripts

c	=	corner
ref	=	reference condition
w	=	wall
∞	=	free-stream condition

References

- [1] Anderson, J. D., Jr., 1989, *Hypersonic and High Temperature Gas Dynamics*, McGraw-Hill, New York.
- [2] Pullin, D. I., and Harvey, J. H., 1976, "A Numerical Simulation of the Rarefied Hypersonic Flat Plate Problem," *J. Fluid Mech.*, **78**, pp. 689–707.
- [3] Vogenitz, F. W., Broadwell, J. E., and Bird, G. A., 1969, "Leading Edge Flow by the Monte Carlo Direct Simulation Technique," 7th Aerospace Science Meeting, AIAA Paper No. 69–141.
- [4] Chun, C.-H., 1991, "Experiments on Separation at a Compression Corner in Rarefied Hypersonic Flow," *Rarefied Gas Dynamics*, A. Beylich, ed., VCH Publishers, New York, pp. 562–569.
- [5] Moss, J., Rault, N., and Price, J. M., 1994, "Direct Monte Carlo Simulations of Hypersonic Viscous Interactions Including Separation," *Rarefied Gas Dynamics: Space Science and Engineering*, B. D. Shzgal and D. P. Weave, eds., Washington, DC.
- [6] Moss, J. N., Price, J. M., and Chun, C. H., 1991, "Hypersonic Rarefied Flow About a Compression Corner—DSMC Simulation and Experiment," 26th Thermophysics Conference, AIAA Paper No. 91-1313.
- [7] Bird, G. A., 1994, *Molecular Gas Dynamics and the Direct Simulation of Gas Flows*, Oxford University Press, New York.
- [8] Robinson, C. D., 1998, "Particle Simulation on Parallel Computers With Dynamic Load Balancing," Ph.D. thesis, Imperial College of Science, Technology and Medicine, U.K.
- [9] Wu, J.-S., Tseng, K.-C., and Kuo, C.-H., 2001, "The Direct Simulation Monte Carlo Method Using Unstructured Adaptive Mesh and Its Application," *Int. J. Numer. Methods Fluids*, accepted for publication.
- [10] Wu, J.-S., Tseng, K.-C., and Yang, T.-J., 2001, "Parallel Implementation of the Direct Simulation Monte Carlo Method Using Unstructured Mesh and Its Application," *Int. J. Numer. Methods Heat Fluid Flow*, submitted for publication.
- [11] Hypermesh, Version 2.0, Altair Computing, Altair Engineering, Inc., Maplelawn, MI.
- [12] Walshaw, C., Cross, M., Everett, M. G., Johnson, S., and McManus, K., 1995, "Partitioning and Mapping of Unstructured Meshes to Parallel Machine Topologies," *Proc. Irregular Parallel Algorithms for Irregularly Structured Problems*, A. Ferreira and J. Rolim, eds., **980**, LNCS, Springer, Berlin, pp. 121–126.